NEOPLASIA
www.neoplasia.com

Volume 10 Number 4 April 2008 pp. 389–398 389

Glucosamine-Bound Near-Infrared Fluorescent Probes with Lysosomal Specificity for Breast Tumor Imaging[1]

Cong Li, Tiffany R. Greenwood and Kristine Glunde

JHU ICMIC Program, The Russell H. Morgan Department of Radiology and Radiological Science, Johns Hopkins University School of Medicine, Baltimore, MD 21205, USA

Abstract

Noninvasive imaging of lysosomes will be useful 1) to elucidate the role of lysosomal parameters in cancer, 2) to diagnose malignant lesions, and 3) to evaluate future lysosome-targeted anticancer therapies. Lysosome-specific labeling of glucosamine-bound near-infrared (NIR) fluorescent probes, IR-1 and IR-2, but not control probe IR-15 without the glucosamine moiety, was observed by fluorescence microscopy in human breast epithelial cell lines. Lysosome labeling and tumor specificity of these NIR probes were investigated by dynamic optical imaging and immunofluorescence staining in human breast tumor xenografts. IR-1 and IR-2 demonstrated faster lysosome labeling rates in highly aggressive MDA-MB-231 and MDA-MB-435 cells compared with less aggressive MCF-7 and nontumorigenic MCF-12A cells. IR-1 and IR-2, but not IR-15, accumulated in human MDA-MB-231, MDA-MB-435, and MCF-7 breast tumor xenografts *in vivo*. IR-2 demonstrated the highest maximum fluorescence and tumor/normal tissue ratios in all tumor models. Specific lysosome labeling from IR-2 *in vivo* was validated by colocalization of the NIR fluorescence with CD63 immunofluorescence in tumor sections. IR-1 and IR-2 demonstrated high lysosome-labeling ability and breast tumor–targeting specificity *in vitro* and *in vivo*. They are promising for diagnosing malignant lesions and may provide a means for evaluating and monitoring future lysosome-targeted anticancer therapies.

Neoplasia (2008) 10, 389–398

Introduction

Lysosomes are membranous organelles found in mammalian cells. For a long time, they were considered to be a *cell dump station*, exclusively involved in the degradation of excess or worn out organelles, food particles, and engulfed viruses or bacteria [1]. The lysosomal lumen is more acidic (≈pH 4.5) than the cytosol (≈pH 7.0) and contains different types of proteases, including the family of cathepsins [2,3]. For example, cathepsins B, L, and D, which are secreted into the extracellular space, actively participate in the digestion of extracellular matrix, thereby enabling the migration, invasion, and metastasis of cancer cells [3,4]. Lysosomes in cancer cells demonstrate significantly different morphology and trafficking compared to lysosomes in normal cells [5]. Our previous studies revealed that, under conditions of acidic extracellular pH, as frequently found in the tumor microenvironment [6], human breast epithelial cells with a high degree of malignancy exhibited larger lysosome sizes, decreased lysosome number, and increased nucleus–lysosome distances than weakly metastatic cells [7]. Mohamed and Sloane [8] also observed that lysosomes in cancer cells at the invasive edges of tumors redistributed from perinuclear to peripheral regions, which may be associated with altered lysosomal trafficking in these cells.

Apart from tumor progression, lysosomes have also been implicated in the lysosomal cell death pathway [5]. Cathepsins released into the cytosol on lysosomal membrane permeabilization can trigger a caspase-independent and Bcl-2–insensitive apoptosis-like cell death pathway in apoptosis-resistant cells, which may provide a new therapeutic strategy for tumors that are resistant to traditional chemotherapy [9]. Groth-Pedersen et al. [10] demonstrated that an early increase

Abbreviations: HMEC, human mammary epithelial cell; NIR, near-infrared; GLUT, glucose transporters; HBSS, Hank's balanced salt solution

Address all correspondence to: Kristine Glunde, JHU ICMIC Program, The Russell H. Morgan Department of Radiology and Radiological Science, Johns Hopkins University School of Medicine, Baltimore, MD 21205. E-mail: kglunde@mri.jhu.edu

[1]This work was supported by R21 CA112216 and P50 CA103175 [Johns Hopkins University *In Vivo* Cellular and Molecular Imaging Center (JHU ICMIC) Program].
Received 20 December 2007; Revised 15 February 2008; Accepted 15 February 2008

Copyright © 2008 Neoplasia Press, Inc. All rights reserved 1522-8002/08/$25.00
DOI 10.1593/neo.07856

in the individual lysosomal volume and in the total lysosomal compartment followed by lysosomal rupture was observed in this cathepsin-mediated apoptosis-like cell death pathway. Therefore, the ability to noninvasively image lysosome morphology and trafficking will be extremely useful 1) to elucidate the role of lysosomal parameters in cancer invasion and metastasis, 2) to provide a means of diagnosing malignant lesions in their early stages, and 3) to evaluate real-time therapeutic response by monitoring lysosomal parameters in future lysosome-targeted anticancer therapies [11–13].

Optical imaging is an emerging noninvasive diagnostic imaging modality, which offers advantages including nonionizing radiation, high sensitivity, low cost, and possibility of real-time image-guided surgical procedures [14,15] compared with conventional techniques such as magnetic resonance imaging and positron emission tomography. Near-infrared tomographic breast imaging demonstrated clinical potential because breast tissue can be easily interrogated by direct contact with NIR sources and detectors. Optical breast imaging studies have validated the high sensitivity for NIR tomographic imaging of intrinsic contrast, and several clinical trials are currently ongoing [16,17]. For future applications of clinical optical imaging, probes that are emissive in the near-infrared region (NIR) of 700 to 900 nm are currently being developed [18–22]. The NIR region is advantageous for *in vivo* optical imaging because background from tissue autofluorescence and absorption from intrinsic chromophores are low, allowing NIR light to penetrate several centimeters into heterogeneous tissues [23].

6-[*N*-(7-Nitrobenz-2-oxa-1,3-diazol-4-yl)amino]-6-deoxyglucose (2-NBDG) [24], pyro-2DG [25], and polyvalent carbocyanine molecular beacons [26], in which fluorophores functionalize the 2-position of glucosamine, were selectively delivered to and accumulated in tumors, possibly due to enhanced glycolysis and an up-regulation of the glucose transporter (GLUT)/hexokinase pathways in cancer cells compared to nonneoplastic cells [27]. Our previous work showed that fluorophores functionalized at the 6-position of glucosamine can specifically label the lysosomes of human mammary epithelial cells (HMECs) *in vitro* [28,29]. Most likely, these modified glucosamines can be used as substrates in cancer cells to biosynthesize highly glycosylated lysosomal proteins [29]. We recently prepared two novel NIR probes: IR-1 and IR-2, in which the NIR chromophore was covalently bound to the 6-position of glucosamine through two different linkers [30] (see Figure 1*A*). These two NIR probes exhibited high quantum yields, low cytotoxicity, reversible pH-dependent fluorescence in the case of IR-2, low aggregation tendency, and efficient cellular uptake in HMEC cultures. In this work, we tested lysosome-labeling capabilities of these two NIR probes in four HMEC lines. The biodistribution, tumor-targeting specificity, and lysosome-labeling abilities of IR-1 and IR-2 in mice bearing human MDA-MB-231, MDA-MB-435, or MCF-7 breast tumor xenografts were also studied. For comparison, control NIR probe IR-15 without covalently bound glucosamine moiety was also evaluated.

Materials and Methods

Preparation of IR-1, IR-2, and Control Probe IR-15

IR-1, IR-2, and IR-15 were synthesized as previously described [30]. Briefly, the hydroxyl-group in the 6-position of glucosamine was converted to a primary amine, which was reacted with 3-(4-hydrophenyl) propionic NHS-ester or 3-(4-iodobutoxy)-phenyl acetate, to offer the two linkers with different lengths. The etherification between the phenol moiety of the linkers and the allyl chloride of IR-783 (Sigma-Aldrich, St. Louis, MO) gave IR-1 and IR-2. Similarly, the control molecule IR-15 was prepared by etherification between phenol and IR-783.

Cell Culture

Four HMEC lines representing different grades of malignancy were obtained from the American Type Culture Collection (Rockville, MD). MCF-12A, a spontaneously immortalized nontumorigenic cell line, was cultured in DMEM-Ham's F12 medium (Invitrogen, Carlsbad, CA) supplemented with 10% horse serum, 100 U/ml penicillin and 100 μg/ml streptomycin (Pen/strep), epidermal growth factor (20 mg/ml), cholera toxin (100 ng/ml), insulin (10 ng/ml), and hydrocortisone (500 ng/ml). MCF-7, an estrogen-sensitive weakly aggressive breast cancer cell line, was cultured in Eagle's minimum essential medium (Mediatech, Herndon, VA) supplemented with 10% fetal bovine serum and antibiotics. The highly aggressive HMEC lines MDA-MB-231 and MDA-MB-435 were maintained in RPMI-1640 medium (Invitrogen) supplemented with 10% fetal bovine serum, 100 U/ml penicillin, and 100 μg/ml streptomycin (Invitrogen). All cells were grown as monolayers in 75-cm^2 culture flasks (Sigma-Aldrich) in a humidified atmosphere of 5% CO_2 in air at 37°C and were harvested when they reached 80% confluence to maintain exponential growth.

Breast Cancer Xenograft Models

All *in vivo* studies were performed in compliance with the National Institutes of Health (NIH) and institutional guidelines established for Animal Core Facilities at the Johns Hopkins University. MDA-MB-231 and MDA-MB-435 tumor xenografts were derived by inoculating 1×10^6 MDA-MB-231 or MDA-MB-435 cells in 0.05 ml of Hank's balanced salt solution (HBSS) into the upper left thoracic mammary fat pad of female severe combined immunodeficiency (SCID) mice anesthetized with a ketamine/acepromazine mixture. Estrogen-dependent MCF-7 tumor growth was supported by a 0.72-mg 17β-estradiol 60-day release pellet (Innovative Research of America, Sarasota, FL) implanted subcutaneously into the back of mice 1 week before tumor inoculation (1×10^6 cells/mouse). Tumor volumes used in the study were 200 to 300 mm^3 and usually developed within 5 weeks of inoculation for MDA-MB-231 and MDA-MB-435 and within 2 months for MCF-7 tumors.

Fluorescence Microscopy

All fluorescence microscopic images were obtained with an Olympus IX81 inverted microscope with epifluorescence and phase contrast optics using 60×/1.42 NA or 100×/1.40 NA oil immersion lenses (Olympus America Inc., Center Valley, PA). The microscope was equipped with a Hamamatsu C9100 EM-CCD digital camera (Hamamatsu Photonics, Bridgewater, NJ) and IPLab 4.0 software (Scanalytics BD Biosciences, Rockville, MD). Near-infrared fluorescence was measured using an indocyanine green (ICG) filter cube (Chroma Set 41030; Chroma Technology Corp., Rockingham, VT; excitation: 775 ± 50 nm and emission: 845 ± 55 nm). Cy3 fluorescence was detected using a Texas Red filter cube (Olympus America Inc.). Phase contrast, NIR, and Alexa Fluor-488 or Cy3 fluorescence images were acquired of the same field of view (FOV).

Immunofluorescence Staining

Human mammary epithelial cells were grown on glass chamber slides (Nalge Nunc, Naperville, IL) to 70% to 80% confluence. A concentration of 20 μM of IR-1, IR-2, or IR-15 in culture medium was added to the cells and was incubated for 8, 24, or 48 hours. The treated cells were washed twice with ice-cold phosphate-buffered saline (PBS) and fixed with 4% paraformaldehyde in PBS for 20 minutes on ice. Cells were washed three times and incubated with 5%

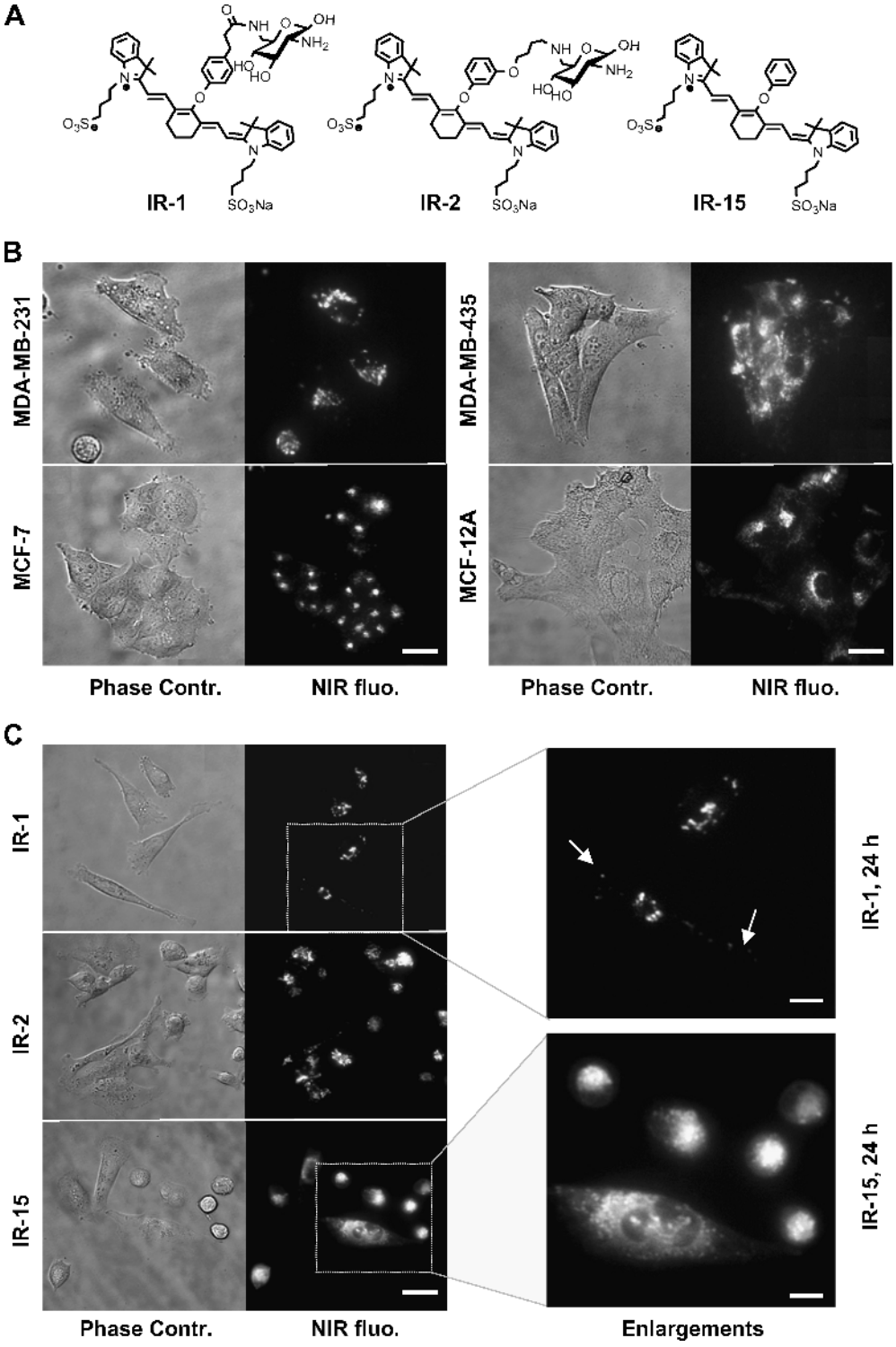

Figure 1. Cellular uptake and localization of NIR probes in live HMEC lines. (A) Chemical structures of IR-1, IR-2, and control molecule IR-15 [30]. (B) NIR fluorescence and phase contrast microscopy images of live MDA-MB-231, MDA-MB-435, MCF-7, and MCF-12A cells after incubation with 20 μM IR-1 for 24 hours. Scale bar, 15 μm. (C) Fluorescence and phase contrast microscopy images of live MDA-MB-231 cells after exposure to 20 μM IR-1, IR-2, and IR-15 for 24 hours. Scale bar, 20 μm. Selected image areas highlighted by a square were enlarged as shown in the right panel of (C). Arrows point the vesicles in the periphery of MDA-MB-231 cells. Scale bar, 10 μm. All images were acquired with a 60× oil immersion lens.

normal donkey serum in PBS for 30 minutes at room temperature. Cells were incubated with a 1:200 dilution (dilution buffer consisting of 0.5% bovine serum albumin and 0.01% sodium azide in PBS) of a monoclonal antibody against CD63 (Abcam, Cambridge, MA) overnight at 4°C. After washing three times with dilution buffer, cells were incubated with a 1:50 dilution of a Cy3-conjugated donkey anti–mouse antibody (Jackson ImmunoResearch Laboratories, West Grove, PA) for 1 hour at room temperature and washed three times with PBS. Cells were mounted with Faramount aqueous mounting medium (Dako, Carpinteria, CA) and ready for imaging.

Lysosome Labeling in Live Cells

Human mammary epithelial cells were seeded on 35-mm glass-bottom culture dishes (14-mm microwell; MatTek, Ashland, MA). After reaching 70% to 80% confluence, culture media containing 0.1 mg/ml Alexa Fluor-488–labeled dextran with a molecular weight of 10 kDa (Molecular Probes, Eugene, OR) was added and incubated for 3 hours. Cells were washed three times with HBSS and continually incubated in normal culture media for 16 hours to achieve lysosome labeling from dextran through the endocytic pathway. After washing three times with HBSS, media with 20 μM IR-1, IR-2, or IR-15 was added, and incubated for another 8 to 24 hours. After washing twice with HBSS, phenol red–free culture media was added to the cells before microscopy studies.

Blocking Studies of Cellular Uptake of NIR Dyes In Vitro

MDA-MB-231 cells cultured in 35-mm glass-bottom culture dishes were preincubated with regular medium, medium supplemented with 50 mM D-glucose, or 1, 2, or 5 mM glucosamine for 1 hour at 37°C, respectively. Glucosamine concentrations greater than 5 mM proved to be toxic and caused cell death. IR-1 or IR-2 with a final concentration of 20 μM was added, and the cells were further incubated for 24 hours at 37°C. At the end of incubation, cells were washed three times with ice-cold HBSS and subjected to microscopy imaging.

In Vivo *and* Ex Vivo *Optical Imaging Studies*

Optical imaging was performed on a Xenogen IVIS 200 small animal imaging system (Xenogen, Alameda, CA) equipped with an indocyanine green (ICG) band pass filter set (810–875 nm). All fluorescence images were acquired with 0.1-second exposure time (FOV, 12.8 cm; *f*/stop, 4; bin, high resolution), and fluorescence intensity was scaled as units of photons per second per centimeter squared per steradian ($p/s/cm^2/sr$). Before imaging, mice were anesthetized, and the fur on the tumor and a large surrounding skin area were shaved to reduce light absorbance and autofluorescent scattering. Serial bright-field photographs and fluorescence images were acquired before and at multiple time points after systemic injection of IR-1, IR-2, or IR-15 (100 nmol/mouse) through the tail vein. During *in vivo* imaging, the tumor and its surrounding normal tissue were chosen as two distinct regions of interest (ROIs). The time-dependent fluorescence intensities in these ROIs were quantified and analyzed by using Living Image 2.5 software (Xenogen). Tumor/normal tissue ratios (*T*/*N*) were calculated by comparing the average fluorescence intensities in the tumor ROI and its surrounding normal tissue ROI. *T*/*N* values at selected time point after injection were normalized to its corresponding value measured preinjection. At the end of *in vivo* imaging studies, the mouse was scarified, and tumor and thigh muscle were excised, sectioned with a thickness of 1.0 mm with a tissue slicer (Braintree Scientific Inc., Braintree, MA), and imaged simultaneously. The fluorescence intensities of *ex vivo* tumor sections were quantified in ImageJ (NIH, Bethesda, MD) and normalized to the value of the muscle.

Biodistribution Studies

Biodistribution studies of IR-1, IR-2, and IR-15 were performed as previously reported [16,31]. Tumor-bearing mice were scarified at 24 hours after intravenous injection of IR-1, IR-2, or IR-15 (100 nmol/mouse). The tumor and major organs were excised and sliced into 3-mm-thick pieces to minimize differences in tissue thickness and depth-dependent nonlinear fluorescence emission. Tissue slices (three to four slices per organ) from at least three mice were imaged with the Xenogen IVIS 200 imaging system. Average fluorescence intensities of tissue sections were quantified by using ImageJ (NIH) and normalized to the value of the thigh muscle from the same animal.

Statistical Analysis

All data are presented as mean ± SD of at least three experiments. We analyzed statistical differences by Student's *t* test (Microsoft Excel 2002, Microsoft Corp, WA). Statistical significance was defined at the level of $P < .05$ (two-tailed).

Results

Cellular Uptake of NIR Probes Was Not Blocked By D-Glucose and Glucosamine in HMEC Lines

Cellular uptakes of IR-1, IR-2, and control molecule IR-15 were investigated in HMECs. A concentration of 20 μM of IR-1 and IR-2 was shown to label HMECs efficiently without causing alterations in cell morphology and doubling time. Figure 1*B* shows fluorescence images of MDA-MB-231, MDA-MB-435, MCF-7, and MCF-12A cells after treatment with 20 μM IR-1 for 24 hours at 37°C. Clear vesicular structures were predominately located in the perinuclear region of cells, and the punctuate staining pattern persisted with increasing fluorescence intensity after incubation for 48 hours. Incubation with IR-2 resulted in labeling similar to IR-1 (Figure 1*C*). However, the intracellular staining pattern from control molecule IR-15 was quite different. As shown in Figure 1*C*, clear vesicular structures labeled by IR-1 or IR-2 were enriched in the perinuclear area, and a few of them were also found in the periphery of MDA-MB-231 cells. In contrast, IR-15 resulted in a homogenously distributed granular staining pattern accompanied by a strong fluorescence background throughout the cytoplasm. To elucidate the cellular uptake mechanism of the glucosamine-bound NIR probes, MDA-MB-231 cells were preincubated with 50 mM D-glucose, or 1, 2, or 5 mM glucosamine before and during treatment with IR-1 or IR-2. The typical intracellular vesicular staining pattern resulting from IR-1 or IR-2 was not affected by either 50 mM D-glucose or up to 5 mM glucosamine (data not shown).

Glucosamine-Bound NIR Probes Label Lysosomes in HMEC Lines

Lysosome labeling from glucosamine-bound NIR probes in live cells was identified by colocalization of the NIR probe with Alexa Fluor-488–conjugated dextran, which was used as a long-term lysosomal fluorescence marker in live cells [32]. Fluorescence microscopy images of live MDA-MB-231 cells after labeling with fluorescent dextran and NIR probes IR-1, IR-2, or IR-15 are shown in Figure 2*A*. Whereas

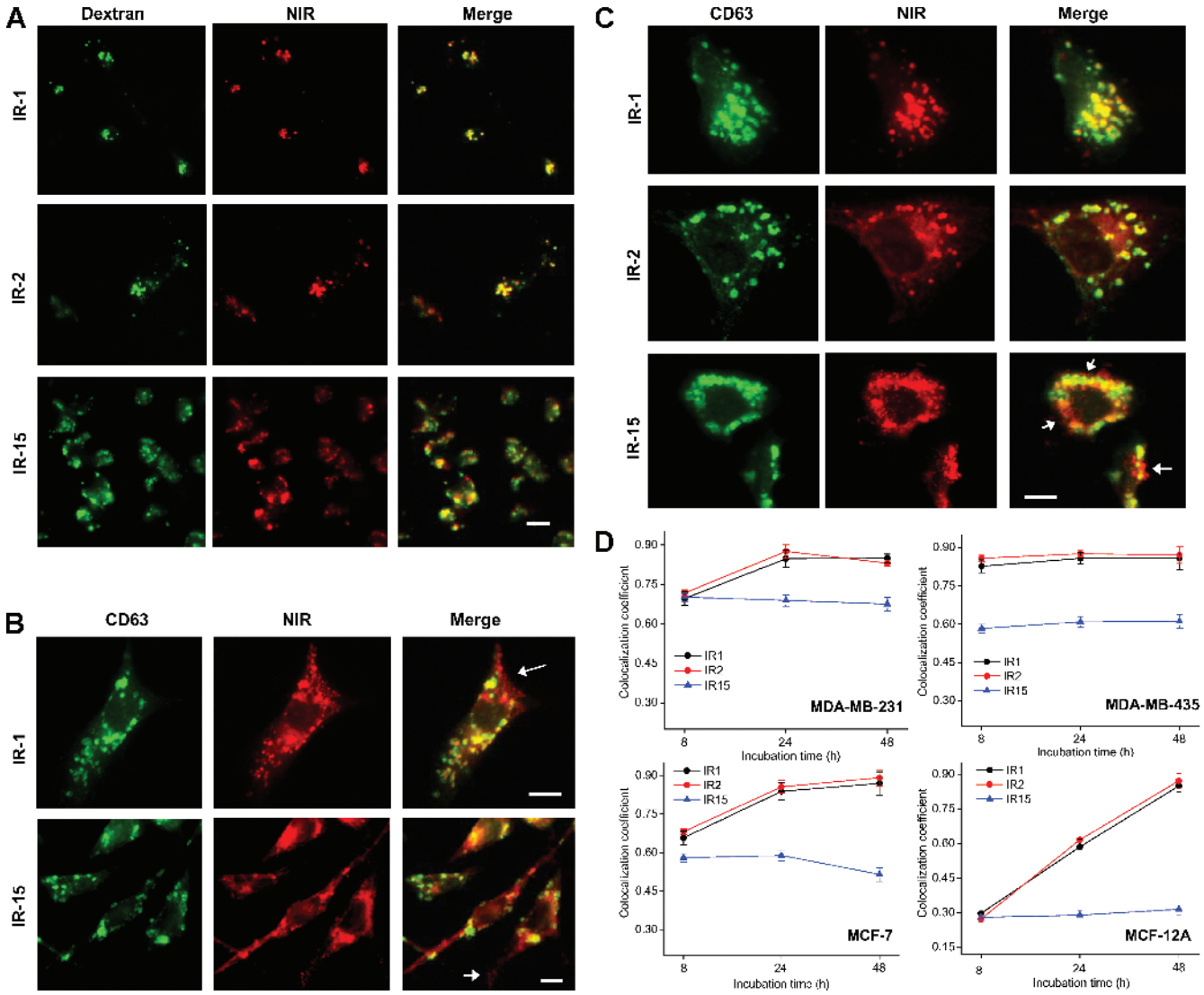

Figure 2. Glucosamine-bound NIR probes demonstrated lysosome specificity in HMEC lines. (A) Representative fluorescence images of live MDA-MB-231 cells treated with the lysosome marker Alexa Fluo-488–conjugated dextran (50 μg/ml) and subsequently with 20 μM IR-1, IR-2, or IR-15 for 24 hours. The NIR fluorescence is displayed in red, and the Alexa Fluo-488 fluorescence is displayed in green. Colocalization of NIR probe and dextran is indicated by yellow in the merged image. Scale bar, 20 μm. These images were acquired with a 60× oil immersion objective. (B) Representative fluorescence images of MDA-MB-231 cells that were treated 20 μM IR-1 or IR-15 for 8 hours, fixed, and followed by immunofluorescence staining with CD63 antibody. These images were acquired with a 100× oil immersion lens. The NIR fluorescence is displayed in red, and the CD63 immunofluorescence is in green. Yellow indicates colocalization of NIR probe and CD63. Arrows point to single-stained vesicle structures at the periphery of cells. Scale bar, 15 μm. (C) Representative fluorescence images of MDA-MB-231 cells that were treated with 20 μM IR-1, IR-2, or IR-15 for 24 hours, fixed, and followed by immunofluorescence staining with CD63 antibody. Arrows point to single-stained vesicle structures. Scale bar, 15 μm. (D) The colocalization coefficients of NIR fluorescence with CD63 immunofluorescence were quantified in HMECs after incubation with NIR probe for 8, 24, or 48 hours. The colocalization coefficients were determined from five to six randomly selected images. All images were acquired with a 40× oil immersion lens, and totally 120 to 200 cells were assessed. Data represent a minimum of three independent experiments. *Data points* indicate the mean; *bars*, SD.

both IR-1 and IR-2 demonstrated excellent colocalization with dextran, only partial colocalization between IR-15 and dextran was observed. To further assess the lysosomal specificity of these NIR probes, HMECs were treated with 20 μM of each NIR probe for 8, 24, or 48 hours before fixation and immunofluorescence staining with CD63 antibody. CD63 is a glycoprotein in the lysosomal membrane and a well-established lysosomal marker [33]. As shown in Figure 2*B*, in addition to the yellow colocalized vesicles in the perinuclear region, single-labeled red vesicles from NIR fluorescence were found in the periphery of MDA-MB-231 cells after incubation for 8 hours. In contrast to IR-1, nonspecific staining from IR-15 resulted in a strong fluorescence background distributed throughout the entire cytoplasm. Compared with the 8-hour incubation, a higher degree of colocalization was observed in cells treated with IR-1 or IR-2 for 24 hours (Figure 2*C*). However, this phenomenon was barely observed in the cells incubated with IR-15. Figure 2*D* shows the time-dependent colocalization coefficients between IR-1, IR-2, or IR-15 and the lysosome marker CD63 in the four HMEC lines. IR-1 and IR-2 demonstrated similar lysosome-labeling

behaviors and exhibited much faster lysosome incorporation rates in the highly aggressive MDA-MB-231 and MDA-MB-435 cell lines as compared with less aggressive MCF-7 and nontumorigenic MCF-12A cells (Figure 2*D*). The colocalization coefficient of IR-15 with CD63 was much lower than that of IR-1 and IR-2 with CD63, and it was independent of the incubation time in all HMEC lines.

Glucosamine-Bound NIR Probes Demonstrated Tumor-Targeting Specificity In Vivo

Whole-body dynamic optical imaging of mice implanted with human breast tumor xenografts was performed after systemic administration of NIR probes. Figure 3 shows representative *in vivo* NIR fluorescence images of MDA-MB-231 tumor–xenografted mice before and at 5, 15, 30, 45, 60, 90, 120, 240, 480, and 1440 minutes after intravenous administration of IR-1, IR-2, or IR-15 (100 nmol/mouse). Specific uptake of IR-1 and IR-2 into the tumor was apparent from highly NIR fluorescent tumors compared to its surrounding normal tissues. However, no remarkable fluorescence was observed in the tumor after the injection of IR-15. At 24 hours after injection of NIR dyes, significant fluorescence was still detected in tumors treated with IR-1 and IR-2. For IR-15, obvious fluorescence was clearly detected in the mouse abdomen but not in the tumor. Near-infrared fluorescence was also detected in the ear, tail, and extremities of the mouse at early time points after administration as evident from Figure 3. Fluorescence intensities in MDA-MB-231, MDA-MB-435, and MCF-7 tumors as a function of time are depicted in Figure 4*A*. Notably, IR-2 demonstrated higher maximum fluorescence intensity and longer residence lifetime than IR-1 and IR-15 in all tumor types. For example, in MDA-MB-231 tumor xenografts, the maximum fluorescence intensities introduced by IR-1, IR-2, and IR-15 were 8.4 ± 0.45, 9.5 ± 0.51, and 4.6 ± 0.33 × 10^{11} p/s/cm^2/sr, and the corresponding $t_{1/2}$ (the time at which the fluorescence intensity in the tumor was reduced to half of its maximum value) were 2.5, 24, and 10.5 hours, respectively. Near-infrared fluorescence intensities in the tumor area also depended on the tumor type. In MCF-7 tumors, the maximum fluorescence intensity resulting from IR-1 or IR-2 was three to five times lower than that in MDA-MB-231 and MDA-MB-435 tumors. Time courses of the fluorescence intensity ratios between tumor and surrounding normal tissue (*T*/*N* value) after systemic administration of NIR probe are shown in Figure 4*B*. IR-2 demonstrated higher *T*/*N* values than IR-1 and IR-15 at all time points in all three tumor models. In contrast, the *T*/*N* values of IR-15 fluctuated around 1.0 for most of the time after administration, demonstrating that IR-15 is not tumor-specific.

Figure 5, *A* and *B*, shows typical NIR fluorescence images, and superimposed photographic and color-coded NIR fluorescence images of SCID mice bearing MDA-MB-435 tumor xenografts, respectively,

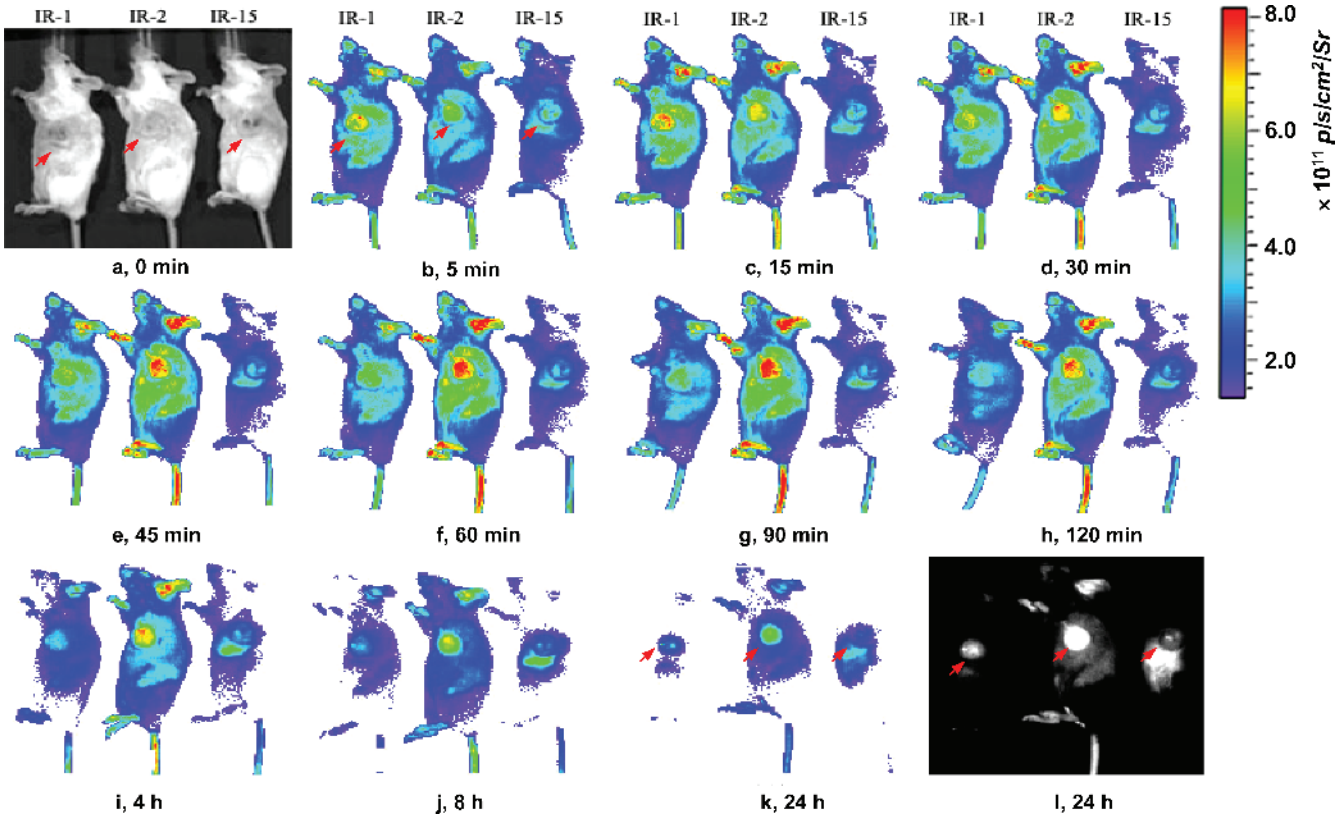

Figure 3. IR-1 and IR-2, but not IR-15, demonstrated targeting specificity to MDA-MB-231 breast tumor xenografts in the *in vivo* dynamic optical imaging studies. *In vivo* optical images of human MDA-MB-231 breast tumor–bearing mice before and after administration of 100 nmol of IR-1, IR-2, or IR-15. (a) Superimposed photography and color-coded fluorescence image of mice before injecting NIR probes. (b–k) Representative color-coded fluorescence images of mice at selected time points after intravenous injection of IR-1, IR-2, or IR-15. (l) Representative NIR fluorescence images of mice at 24 hours after injection of IR-1, IR-2, or IR-15. The arrows point the position of tumors in the mice. All images were acquired on a Xenogen IVIS 200 small animal imaging system with an ICG excitation and emission filter set. FOV, 12.8 cm; *f*/stop, 4; bin, high resolution; exposure time, 0.1 second. Arrows point the position of the tumor xenograft.

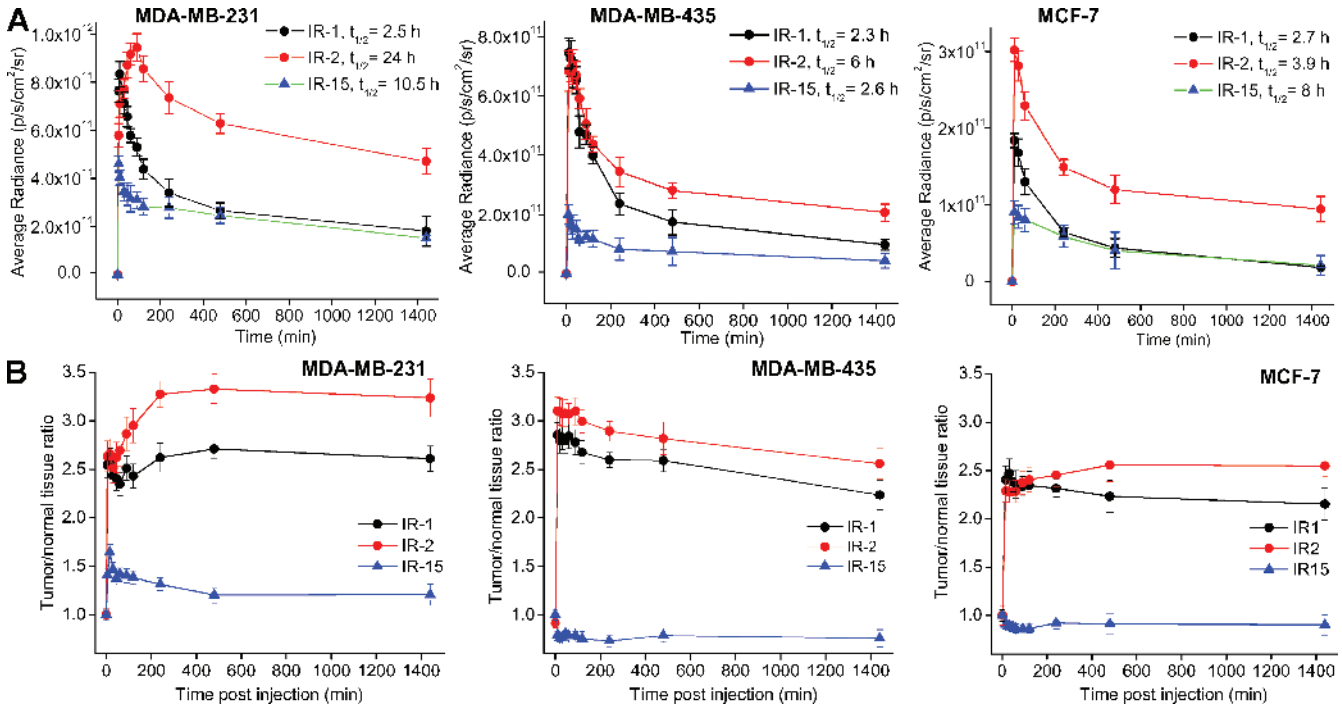

Figure 4. Quantification and kinetics of *in vivo* targeting characteristics of NIR probes in MDA-MB-231, MDA-MB-435, and MCF-7 tumor-bearing SCID mice. (A) Time course of *in vivo* fluorescence intensities in three different types of breast tumor xenografts measured as units of p/s/cm^2/sr. Near-infrared probes were intravenously injected with a dosage of 100 nmol/mouse. $t_{1/2}$ represents the time at which the tumoral fluorescence intensity has decreased to half of its maximum value. (B) Time course of *T/N* calculated for the three types of breast tumor xenografts after intravenous injection of IR-1, IR-2, or IR-15 (100 nmol/mouse). *T/N* values were normalized to preinjection background levels measured before NIR probe injection. Data are expressed as mean ± SD (n = 3 mice per group).

at 24 hours after injection of IR-1, IR-2, or IR-15. Comparable to the MDA-MB-231 tumor model, IR-1 and IR-2 resulted in efficient tumoral NIR fluorescence enhancement in MDA-MB-435 tumor xenografts. The most intense fluorescence from IR-15 was located in the pelvic area, and originated from the liver as evident from the *ex vivo* studies. The tumors shown in Figure 5, *A* and *B*, were excised and sectioned at 24 hours after injection. Fluorescence imaging of these fresh tumor sections (Figure 5*C*) revealed a heterogeneous intratumoral distribution of all NIR probes, with IR-2 exhibiting the most intense fluorescence. The biodistribution of IR-1, IR-2, and IR-15 at 24 hours after injection was investigated in tumor-xenografted mice as shown in Figure 5*D*. Tumor uptakes of IR-1 and IR-2 were two- to four-fold higher than that of IR-15. Apart from the tumor, IR-1 and IR-2 were also retained in organs including liver and intestine, but little of these dyes were detected in muscle, brain, spleen, and blood. IR-15 predominately accumulated in the liver, in which the average fluorescence intensity was eight times higher compared to that of IR-1 or IR-2. IR-15 also demonstrated higher fluorescence intensity in the gastrointestinal system compared to IR-1 or IR-2.

Glucosamine-Bound NIR Probes Label Lysosomes in Tumor Xenografts

The lysosome-labeling ability of these NIR probes was assessed by CD63 immunofluorescence staining of tumor sections after *in vivo* imaging studies. As shown in Figure 6, *A* and *C*, partial and more complete colocalization between IR-2 and CD63 was demonstrated at 8 and 24 hours after injection, respectively. However, NIR fluorescence from IR-1 (data not shown) and IR-15 was much lower in tumor sections than that from IR-2 (Figure 6*B*). The colocalization coefficient of each NIR probe in MDA-MB-231 tumor xenografts was quantified as presented in Figure 6*D*. IR-2 exhibited significantly higher colocalization coefficients than IR-15 at both 8 and 24 hours after injection. Comparable values for the *ex vivo* fluorescence colocalization between IR-2 and CD63 were also obtained in MDA-MB-435 and MCF-7 breast tumor xenografts (data not shown).

Discussion

We synthesized two glucosamine-bound NIR fluorescent probes and evaluated their lysosomal-labeling capability and tumor-targeting specificity *in vitro* and *in vivo*. These probes can also potentially be used for *in vivo* subcellular lysosome imaging with minimally invasive intravital microscopy. The ability to optically image lysosomes *in vivo* will further our understanding of the role of lysosomes in tumor invasion and metastasis [7], provide a future means of diagnosing malignant cancers, and help in developing lysosome-targeted anticancer therapies [11–13] that exploit the lysosomal cell death pathway [5].

2-[^{18}F] Fluoro-2-deoxy- D-glucose (FDG) has been successfully used in positron emission tomography to image tumors in the clinic for more than two decades [34]. FDG accumulates in tumors due to the upregulated GLUTs in cancer cells and the lacking hydroxyl group at the 2-position which prevents its further glycolysis [34]. Near-infrared probes that are analogous to FDG, such as pyro-2DG [25], polyvalent carbocyanine beacons [26], and Cy5.5-2DG [35] also demonstrated specific accumulation in various tumor xenograft models, although their uptake mechanism remains controversial. Functionalization of fluorophore at the 6-position of glucosamine such as 6-NBDG demonstrated a similar cellular uptake through GLUT1 as

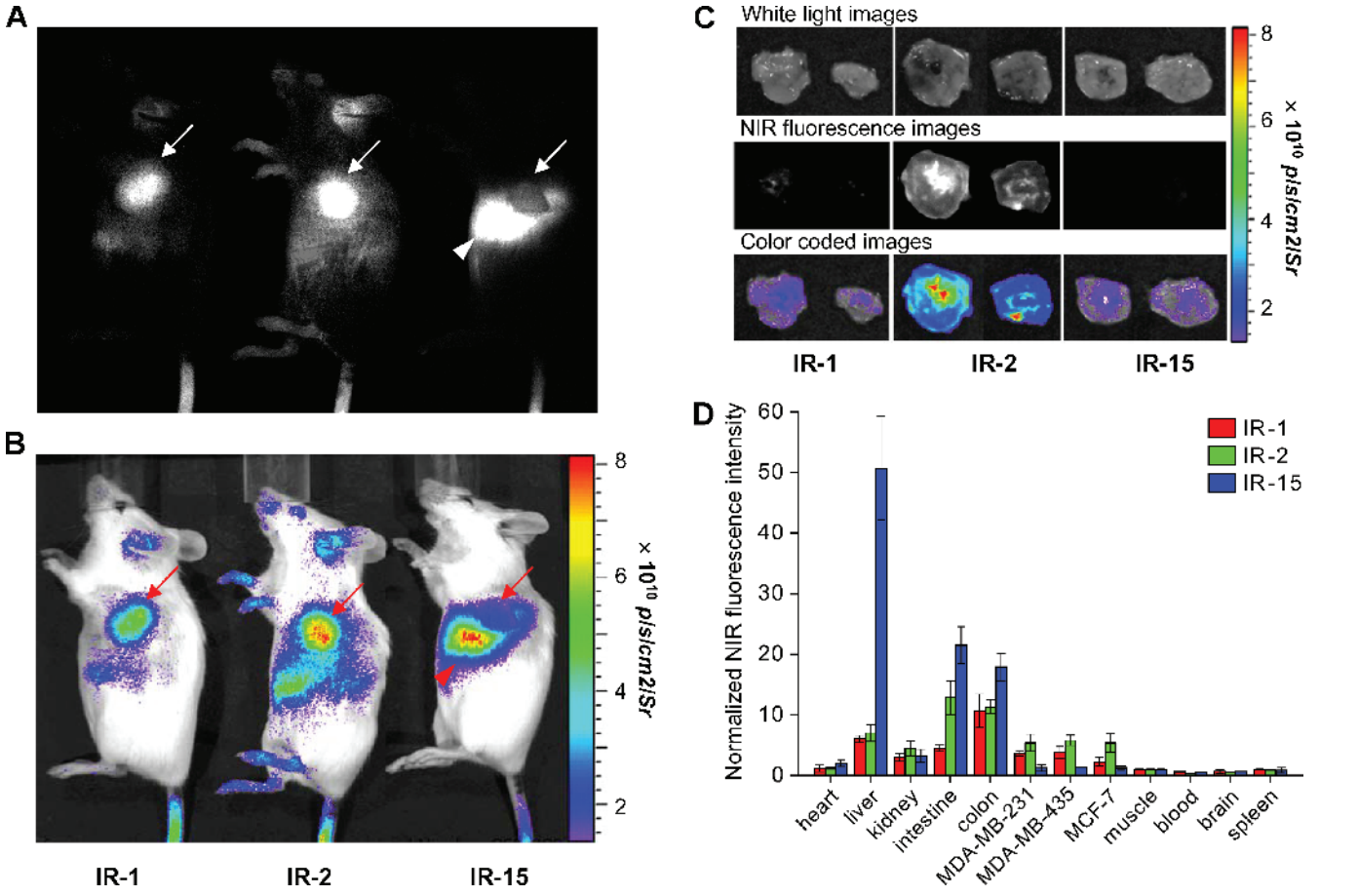

Figure 5. Glucosamine-bound NIR probes IR-1 and IR-2 demonstrated targeting specificity to human MDA-MB-231, MDA-MB-435, and MCF-7 breast tumor xenografts. (A) Representative NIR fluorescence image of MDA-MB-435 tumor bearing mice at 24 hours after injection of 100 nmol IR-1, IR-2, or IR-15. (B) Superimposed photography and color-coded fluorescence image of the mice shown in panel (A). Arrows point the position of the tumor xenograft; arrowheads point the position of the liver. (C) Representative *ex vivo* white light, fluorescence, and color-coded fluorescence images of MDA-MB-435 tumor sections with a thickness of 1.0 mm at 24 hours after injection of IR-1, IR-2, or IR-15 (100 nmol/mouse). (D) Biodistribution of IR-1, IR-2, and IR-15 in MDA-MB-231, MDA-MB-435, and MCF-7 tumor-bearing mice at 24 hours after systemic injection into the tail vein. The fluorescence intensities in the tissue sections were normalized to that of muscle. Data are expressed as mean ± SD (n = 3 for each type of tumor xenograft).

2-NBDG [36], indicating that 6-position–modified glucosamines such as IR-1 and IR-2 may also be taken up through GLUT1. However, our *in vitro* blocking studies showed that the cellular uptake of IR-1 and IR-2 in MDA-MB-231 cells was not significantly blocked by 50 mM D-glucose, which suggests that IR-1 and IR-2 are not taken up into breast cancer cells through GLUTs. The uptake of these two NIR probes was not blocked in the presence of up to 5 mM glucosamine either. Higher concentrations of glucosamine could not be tested in these blocking studies because of its toxicity at higher concentrations.

The lysosome-labeling capability of IR-1 and IR-2 in HMECs cultures was demonstrated by colocalization of NIR fluorescence with fluorescence from lysosomal markers in live and fixed cells. The faster lysosome-labeling rates of IR-1 and IR-2 observed in the two highly aggressive MDA-MB-231 and MDA-MB-435 breast cancer cell lines compared to the less aggressive MCF-7 cell line and nontumorigenic MCF-12A cell line may be explained by differences in protein glycosylation, which is important in tumorigenesis and progression to metastatic disease [37,38].

To elucidate the role of the glucosamine moiety for lysosome- and tumor-labeling specificity, we compared IR-1 and IR-2 to a control NIR probe, IR-15, in which the glucosamine was replaced with a biochemically inert benzene ring. In contrast to the clear vesicle structures predominately found in the perinuclear region of cells treated with IR-1 or IR-2, a homogenously granular staining pattern with a strong fluorescent background in the cytoplasm was observed in the cells exposed to IR-15. The time independence of the partial IR-15 colocalization with lysosomes in HMECs further supports that glucosamine-bound IR–1/2 and control molecule IR-15 might be taken up by entirely different cellular transport and trafficking pathways. It is obvious that the glucosamine moiety in IR-1 and IR-2 was crucial in conferring lysosome specificity as evident from the high degree of colocalization of IR-1 and IR-2 with lysosomal markers.

Our *in vivo* experiments demonstrated an excellent tumor specificity of the glucosamine-bound NIR probes IR-1 and IR-2, which was apparent from high tumoral fluorescence intensity and *T*/*N* values after systemic administration in breast tumor–xenografted mice. Although IR-1 and IR-2 demonstrated similar lysosomal labeling properties in the cell culture studies, our dynamic *in vivo* imaging studies indicated that IR-1 underwent a more rapid excretion rate in these animal models, possibly leading to the lower *T*/*N* values when compared

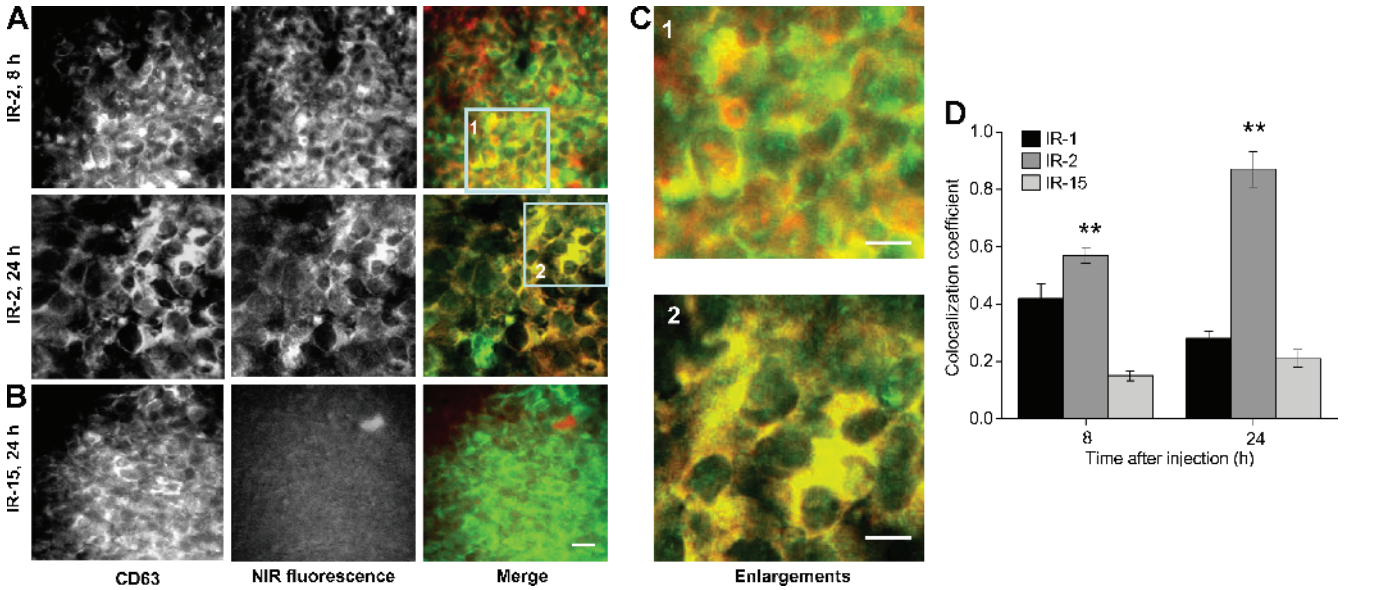

Figure 6. IR-2 specifically labeled lysosomes in MDA-MB-231 human breast tumor xenografts. (A) Representative fluorescence images of *ex vivo* MDA-MB-231 breast tumor sections at 8 (upper panel) and 24 hours (lower panel) after injection of IR-2 (100 nmol/mouse) and after immunofluorescence staining with CD63 antibody. The NIR fluorescence and CD63 immunofluorescence are displayed in red and green, respectively. (B) Representative fluorescence images of MDA-MB-231 tumor sections at 24 hours after injection of IR-15 (100 nmol/mouse; scale bar, 20 μm). (C) Enlargements of corresponding image areas highlighted by a square in panel (A). Scale bars, 10 μm. (D) Colocalization coefficients of the NIR fluorescence with CD63 immunofluorescence in MDA-MB-231 tumor sections at 8 and 24 hours after injection of IR-1, IR-2, or IR-15 (100 nmol/mouse). Eight randomly selected images from at least three tumor-xenografted mice were analyzed. The colocalization coefficients were normalized to that in tumors treated with IR-15. Data are expressed as mean ± SD. Bars, SD. $^{**}P < .01$. Bars, as compared with tumors treated with IR-15.

to IR-2. Structurally, the overall positive charges of IR-2 in the physiological pH range may facilitate its association with negatively charged albumin through electrostatstic binding, which may prolong its circulation lifetime and result in evident fluorescence in the highly vascularized ears, tail, and extremities of the mouse at early time points after administration. Both IR-1 and IR-2 demonstrated three- to five-fold higher fluorescence intensities in MDA-MB-231 and MDA-MB-435 tumors compared to MCF-7 tumors at any given time point (0–24 hours) after systemic administration. This result may be explained by increased protein glycosylation in the highly aggressive MDA-MB-231 and MDA-MB-435 tumors as compared with the less aggressive MCF-7 tumors [37,38]. Given the performance of IR-1 and IR-2 in the *in vivo* studies, these glucosamine-bound NIR probes, especially IR-2, may not only be used to diagnose breast tumors in their early stages but may also provide a means of differentiating aggressive tumors from less aggressive lesions by evaluating the fluorescence intensity in the tumor site. IR-15 without the glucosamine moiety did not demonstrate any tumor specificity in the three tumor xenograft models, and it predominantly accumulated in the liver. As the liver is known to accumulate lipophilic molecules [39,40], our data indicate that conjugating glucosamines with multiple hydrophilic groups to NIR fluorophores can substantially improve the pharmacokinetics and pharmacodynamic behavior of these NIR fluorophores. The retention of IR-1 and IR-2 in the liver, kidney, and gastrointestinal system was most likely due to the excretion of these NIR probes through both the renal and hepatobiliary pathways because NIR fluorescence was also detected in the urine and feces of these mice at 24 hours after tail vein injection (data not shown). Lysosomal immunofluorescence staining revealed that IR-2 localized to the lysosomes in human breast tumor xenografts after systemic administration. The lysosome labeling from IR-2 in tumors, as identified by the colocalization coefficient, was time-dependent and reached maximal values at 24 hours after injection. These combined *ex vivo* immunofluorescence data suggest that the tumor specificity of IR-2 *in vivo* may partially result from its efficient lysosome labeling.

In conclusion, both glucosamine-bound NIR probes IR-1 and IR-2 demonstrated efficient lysosome labeling in breast cancer cell cultures, as well as excellent tumor-targeting specificity and lysosome labeling in human breast cancer xenografts *in vivo*. IR-2 also provided very good detection sensitivity and high *T*/*N* ratio. These probes will be extremely helpful in understanding the role of lysosome morphology and trafficking in breast cancer invasion and metastasis *in vivo*. Monitoring lysosomal parameters using IR-1 and IR-2 may further provide a means for early diagnosis of malignant lesions and for evaluating the real-time response to lysosome-targeted or lysosome-affecting anticancer therapies.

Acknowledgments

We thank Zaver M. Bhujwalla for helpful scientific discussions.

References

[1] de Duve C (1983). Lysosomes revisited. *Eur J Biochem* **137**, 391–397.
[2] Rawlings ND, Morton FR, and Barrett AJ (2006). MEROPS: the peptidase database. *Nucleic Acids Res* **34**, D270–D272.
[3] Gocheva V and Joyce JA (2007). Cysteine cathepsins and the cutting edge of cancer invasion. *Cell Cycle* **6**, 60–64.
[4] Mignatti P and Rifkin DB (1993). Biology and biochemistry of proteinases in tumor invasion. *Physiol Rev* **73**, 161–195.
[5] Kroemer G and Jaattela M (2005). Lysosomes and autophagy in cell death control. *Nat Rev Cancer* **5**, 886–897.
[6] Gatenby RA, Gawlinski ET, Gmitro AF, Kaylor B, and Gillies RJ (2006). Acid-mediated tumor invasion: a multidisciplinary study. *Cancer Res* **66**, 5216–5223.

[7] Glunde K, Guggino SE, Solaiyappan M, Pathak AP, Ichikawa Y, and Bhujwalla ZM (2003). Extracellular acidification alters lysosomal trafficking in human breast cancer cells. *Neoplasia* **5**, 533–545.

[8] Mohamed MM and Sloane BF (2006). Cysteine cathepsins: multifunctional enzymes in cancer. *Nat Rev Cancer* **6**, 764–775.

[9] Daugaard M, Kirkegaard-Sorensen T, Ostenfeld MS, Aaboe M, Hoyer-Hansen M, Orntoft TF, Rohde M, and Jaattela M (2007). Lens epithelium-derived growth factor is an Hsp70-2 regulated guardian of lysosomal stability in human cancer. *Cancer Res* **67**, 2559–2567.

[10] Groth-Pedersen L, Ostenfeld MS, Hoyer-Hansen M, Nylandsted J, and Jäättelä M (2007). Vincristine induces dramatic lysosomal changes and sensitizes cancer cells to lysosome-destabilizing siramesine. *Cancer Res* **67**, 2217–2225.

[11] Kusuzaki K, Murata H, Matsubara T, Satonaka H, Wakabayashi T, Matsumine A, and Uchida A (2007). Review. Acridine orange could be an innovative anticancer agent under photon energy. *In Vivo* **21**, 205–214.

[12] Mijatovic T, Mathieu V, Gaussin JF, De Neve N, Ribaucour F, Van Quaquebeke E, Dumont P, Darro F, and Kiss R (2006). Cardenolide-induced lysosomal membrane permeabilization demonstrates therapeutic benefits in experimental human non–small cell lung cancers. *Neoplasia* **8**, 402–412.

[13] Ichinose S, Usuda J, Hirata T, Inoue T, Ohtani K, Maehara S, Kubota M, Imai K, Tsunoda Y, Kuroiwa Y, et al. (2006). Lysosomal cathepsin initiates apoptosis, which is regulated by photodamage to Bcl-2 at mitochondria in photodynamic therapy using a novel photosensitizer, ATX-s10 (Na). *Int J Oncol* **29**, 349–355.

[14] Shah N, Cerussi A, Eker C, Espinoza J, Butler J, Fishkin J, Hornung R, and Tromberg B (2001). Noninvasive functional optical spectroscopy of human breast tissue. *Proc Natl Acad Sci USA* **98**, 4420–4425.

[15] Koyama Y, Hama Y, Urano Y, Nguyen DM, Choyke PL, and Kobayashi H (2007). Spectral fluorescence molecular imaging of lung metastases targeting HER2/*neu*. *Clin Cancer Res* **13**, 2936–2945.

[16] Pogue BW, Poplack SP, McBride TO, Wells WA, Osterman KS, Osterberg UL, and Paulsen KD (2001). Quantitative hemoglobin tomography with diffuse near-infrared spectroscopy: pilot results in the breast. *Radiology* **218**, 261–266.

[17] Ntziachristos V, Yodh AG, Schnall MD, and Chance B (2002). MRI-guided diffuse optical spectroscopy of malignant and benign breast lesions. *Neoplasia* **4**, 347–354.

[18] Hama Y, Koyama Y, Choyke PL, and Kobayashi H (2007). Two-color *in vivo* dynamic contrast-enhanced pharmacokinetic imaging. *J Biomed Opt* **12**, 034016.

[19] Bremer C, Tung CH, Bogdanov A Jr, and Weissleder R (2002). Imaging of differential protease expression in breast cancers for detection of aggressive tumor phenotypes. *Radiology* **222**, 814–818.

[20] Koyama Y, Barrett T, Hama Y, Ravizzini G, Choyke PL, and Kobayashi H (2007). *In vivo* molecular imaging to diagnose and sub-type tumors via receptor-targeted optically-labeled monoclonal antibodies. *Neoplasia* **9**, 1021–1029.

[21] Zhang G-J, Chen TB, Bednar B, Connolly BM, Hargreaves R, Sur C, and Williams DL (2007). Optical imaging of tumor cells in hollow fibers: evaluation of anti-tumor activities of anti-cancer drugs and target validation. *Neoplasia* **9**, 652–661.

[22] Pham W, Xie J, and Gore JC (2007). Tracking the migration of dendritic cells by *in vivo* optical imaging. *Neoplasia* **9**, 1130–1137.

[23] Achilefu S (2004). Lighting up tumors with receptor-specific optical molecular probes. *Technol Cancer Res Treat* **3**, 393–409.

[24] O'Neil RG, Wu L, and Mullani N (2005). Uptake of a fluorescent deoxyglucose analog (2-NBDG) in tumor cells. *Mol Imaging Biol* **7**, 388–392.

[25] Zhang M, Zhang Z, Blessington D, Li H, Busch TM, Madrak V, Miles J, Chance B, Glickson JD, and Zheng G (2003). Pyropheophorbide 2-deoxyglucosamide: a new photosensitizer targeting glucose transporters. *Bioconjug Chem* **14**, 709–714.

[26] Ye Y, Bloch S, Kao J, and Achilefu S (2005). Multivalent carbocyanine molecular probes: synthesis and applications. *Bioconjug Chem* **16**, 51–61.

[27] Gambhir SS (2002). Molecular imaging of cancer with positron emission tomography. *Nat Rev Cancer* **2**, 683–693.

[28] Glunde K, Guggino SE, Ichikawa Y, and Bhujwalla ZM (2003). A novel method of imaging lysosomes in living human mammary epithelial cells. *Mol Imaging* **2**, 24–36.

[29] Glunde K, Foss CA, Takagi T, Wildes F, and Bhujwalla ZM (2005). Synthesis of 6′-*O*-lissamine-rhodamine B-glucosamine as a novel probe for fluorescence imaging of lysosomes in breast tumors. *Bioconjug Chem* **16**, 843–851.

[30] Li C, Greenwood TR, Bhujwalla ZM, and Glunde K (2006). Synthesis and characterization of glucosamine-bound near-infrared probes for optical imaging. *Org Lett* **8**, 3623–3626.

[31] Zhang Z, Liang K, Bloch S, Berezin M, and Achilefu S (2005). Monomolecular multimodal fluorescence–radioisotope imaging agents. *Bioconjug Chem* **16**, 1232–1239.

[32] Rejman J, Bragonzi A, and Conese M (2005). Role of clathrin- and caveolae-mediated endocytosis in gene transfer mediated by lipo- and polyplexes. *Mol Ther* **12**, 468–474.

[33] Metzelaar MJ, Wijngaard PL, Peters PJ, Sixma JJ, Nieuwenhuis HK, and Clevers HC (1991). CD63 antigen. A novel lysosomal membrane glycoprotein, cloned by a screening procedure for intracellular antigens in eukaryotic cells. *J Biol Chem* **266**, 3239–3245.

[34] Di Chiro G (1987). Positron emission tomography using [^{18}F] fluorodeoxyglucose in brain tumors. A powerful diagnostic and prognostic tool. *Invest Radiol* **22**, 360–371.

[35] Cheng Z, Levi J, Xiong Z, Gheysens O, Keren S, Chen X, and Gambhir SS (2006). Near-infrared fluorescent deoxyglucose analogue for tumor optical imaging in cell culture and living mice. *Bioconjug Chem* **17**, 662–669.

[36] Loaiza A, Porras OH, and Barros LF (2003). Glutamate triggers rapid glucose transport stimulation in astrocytes as evidenced by real-time confocal microscopy. *J Neurosci* **23**, 7337–7342.

[37] Brockhausen I (2006). Mucin-type *O*-glycans in human colon and breast cancer: glycodynamics and functions. *EMBO Rep* **7**, 599–604.

[38] Couldrey C and Green JE (2000). Metastases: the glycan connection. *Breast Cancer Res* **2**, 321–323.

[39] Li C, Li YX, Law GL, Man K, Wong WT, and Lei H (2006). Fast water–exchange Gd^{3+}–(DO3A-like) complex functionalized with aza-15-crown-5 showing prolonged residence lifetime *in vivo*. *Bioconjug Chem* **17**, 571–574.

[40] Schuhmann-Giampieri G, Schmitt-Willich H, Press WR, Negishi C, Weinmann HJ, and Speck U (1992). Preclinical evaluation of Gd-EOB–DTPA as a contrast agent in MR imaging of the hepatobiliary system. *Radiology* **183**, 59–64.